6 High Temperature Alloys

For long term applications at high temperatures, the Ti-6Al-4V alloy is limited to about 400°C. For higher temperatures, titanium alloys (such as Ti-6242 and IMI 834) have been formulated according to the following general principles.

The diffusion rates in the β phase are about two orders of magnitude faster than in the α phase. Therefore, the volume fraction of β phase is reduced in these high temperature alloys as compared to Ti-6Al-4V, for example at 800°C the Ti-6Al-4V alloy contains about 15 vol% β phase whereas the Ti-6242 alloy contains about 10 vol% and the IMI 834 alloy only about 5 vol%. This decrease in volume fraction of β phase in Ti-6242 and IMI 834 is achieved by reducing the total content of β stabilizing elements and by alloying in addition to the 6% Al the elements Sn and Zr which act as α stabilizing elements (see Table 2.6 and Sect. 2.5). Furthermore, the β stabilizing element vanadium is replaced by Mo and Nb which are slower diffusing elements [2.33]. In addition, the content of Fe, which is a very strong β stabilizer and also leads to very fast diffusion rates in α titanium (see Sect. 2.9.1), is reduced especially in IMI 834 to the very low level of 0.05%.

Due to the reduction in volume fraction of β phase, the thickness of the "β lamellae" in a colony structure is reduced in many areas to zero, i.e. only low angle boundaries are left separating parallel α lamellae. In this case, easy slip is possible over long distances with the negative consequences outlined in Sect. 5.2, especially for fatigue strength (HCF and LCF). To create new obstacles to dislocation motion at the α/α lamellae boundaries, silicon is added to high temperature alloys (about 0.1-0.5%). Silicon forms with titanium the intermetallic compound Ti_5Si_3 or in the presence of zirconium the compound $(Ti,Zr)_5Si_3$. This intermetallic compound has a complicated crystallographic structure. Therefore, the silicides are incoherent with respect to β and α and precipitate at the α/β lamellae boundaries and at grain boundaries. An example of the microstructure in a lamellar area is shown in Fig. 6.1 for the IMI 834 alloy. It can be seen that the former "β lamellae" have dissolved and $(Ti,Zr)_5Si_3$ particles have precipitated at the α/α plate boundaries which otherwise consist only of arrays of dislocations (low angle boundaries).

Since coherent precipitates are effective barriers for dislocation glide and climb, the volume fraction of Ti_3Al (α_2) particles is increased in high temperature titanium alloys, mainly due to the addition of Sn which promotes the formation of α_2, see Sect. 2.8.1. For example, the solvus temperature for α_2 in Ti-6Al-4V is around 550-600°C, in Ti-6242 around 650°C, and in IMI 834 around 750°C. In contrast to Ti-6Al-4V, the standard final heat treatment in Ti-6242 and IMI 834 is always an aging treatment in the ($\alpha+\alpha_2$) phase region, i.e. 8h 595°C for Ti-6242 and 2h 700°C for IMI 834. An example of the α_2 particles in IMI 834 was shown in Fig. 2.20 (Sect. 2.8.1).

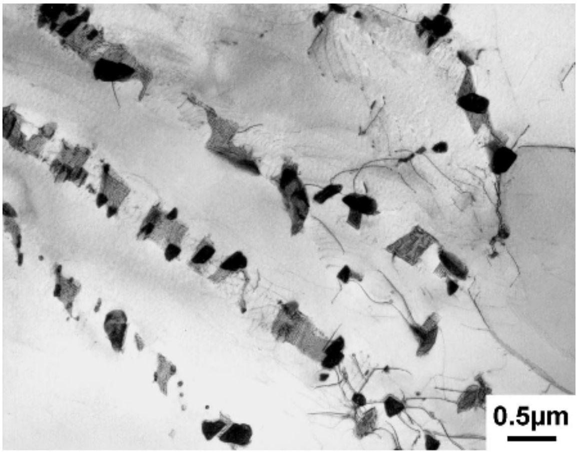

Fig. 6.1. Precipitation of $(Ti,Zr)_5Si_3$ particles at α/α plate boundaries in lamellar regions of bi-modal microstructures of IMI 834, aged 2 h at 700°C, TEM

6.1
Processing and Microstructure

The processing routes to generate different microstructures, for example fully lamellar or bi-modal microstructures, in high temperature titanium alloys (Ti-6242, IMI 834) are the same processing routes as those outlined in Chap. 5 (Sect. 5.1) for $\alpha+\beta$ titanium alloys. The only additional feature important for the processing route of high temperature titanium alloys is the solvus temperature of the silicides in relation to the other temperatures in the processing route. This is shown qualitatively in Fig. 6.2 on the example of the processing route for bi-modal microstructures. This processing route was selected as example, because the bi-modal microstructure is the most commonly used microstructure in high temperature titanium alloys for applications in the compressor section of aero-engines. From Fig. 6.2 it can be seen that both the deformation temperature (step II) and the recrystallization annealing temperature (step III) are above the solvus temperature for the silicides. Therefore, all the silicon is in solid solution at these temperatures (silicon partitions nearly exclusively into the β phase). The silicon is then precipitated as silicides at the lamellae boundaries in the lamellar regions of the bi-modal microstructure (Fig. 6.1) during the final annealing treatment. Also shown in Fig. 6.2 is the solvus temperature for the Ti_3Al (α_2) precipitates demonstrating that the final annealing treatment is performed in the ($\alpha+\alpha_2$) phase region and is, therefore, an aging treatment for the α phase. It should be mentioned that due to the alloying element partitioning effect (see Sect. 5.1.2) the volume fraction of α_2 particles is much higher within the α_p grains than within the α plates in the lamellar areas of the bi-modal microstructures [6.1].

Although the recently developed high temperature alloy Ti-1100 (Ti-6Al-2.7Sn-4Zr-0.4Mo-0.45Si) is no longer on the market, this alloy might serve as processing example for the case that the solvus temperature for $(Ti,Zr)_5Si_3$ is higher (1040°C) than the β transus (1015°C). In this case, the deformation in the (α+β) phase field has to be done in the presence of relatively coarse $(Ti,Zr)_5Si_3$ particles. In addition, the bi-modal microstructures would contain relatively coarse silicides because the recrystallization annealing treatment in the (α+β) phase field to create the bi-modal microstructure would be below the solvus temperature for the silicides. So, for Ti-1100 the alloy producer recommended to use for (α+β) processed material a subsequent recrystallization treatment in the β phase field above the solvus temperature of the silicides (β annealing) or to use β processing above the silicides solvus temperature leading in both cases to fully lamellar microstructures without coarse silicides.

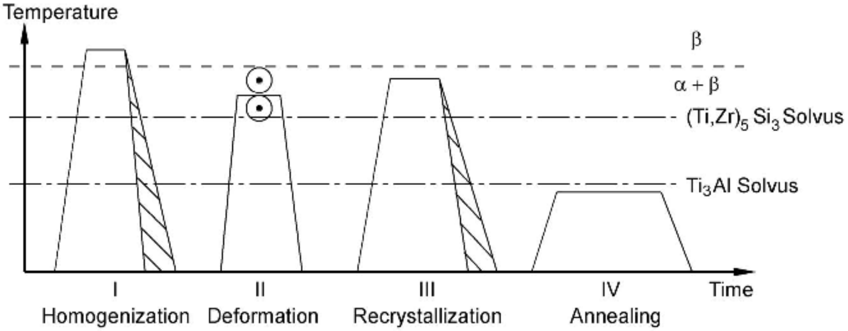

Fig. 6.2. Processing route for bi-modal microstructures of high temperature titanium alloys including the solvus temperatures for $(Ti,Zr)_5Si_3$ and Ti_3Al (schematically)

6.2
Microstructure and Mechanical Properties

The dependence of the mechanical properties at room temperature on cooling rate either from the β phase field in case of fully lamellar microstructures or from the recrystallization annealing temperature in the (α+β) phase field in case of bi-modal microstructures was discussed in detail on the example of fully lamellar microstructures in Sect. 5.2.1 and summarized in Table 5.6 by the row "Small α Colonies and α Lamellae". This cooling rate also has a dominating influence on the mechanical properties at elevated temperatures. This is shown in Fig. 6.3 for the yield stress of the Ti-6242 alloy using the bi-modal microstructure (α_p about 20 vol%) as example [6.1]. It can be seen that the dependence of yield stress on cooling rate is similar for both the high temperature tests (450°C, 510°C) and the room temperature tests. The dashed lines in Fig. 6.3 point out that for the slow cooling rate of 1°C/min the bi-modal microstructure is changed to a fully equiaxed microstructure as described in Sect. 5.1.3. Comparing Fig. 6.3 with Fig. 5.18, it can be seen that qualitatively the dependence of yield stress on cooling rate is similar for bi-modal and fully lamellar microstructures in accordance with the overall discussion on slip length (Fig. 5.17).

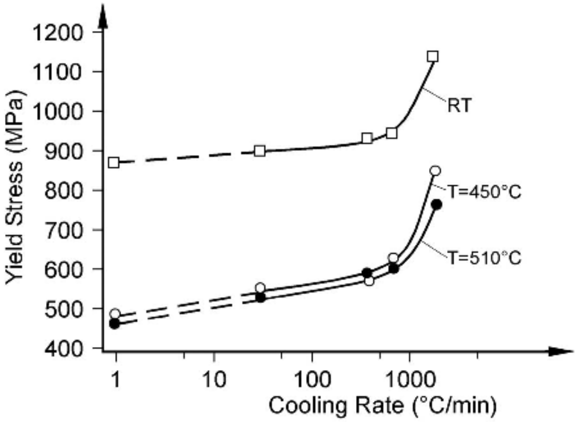

Fig. 6.3. Yield stress at different temperatures as a function of cooling rate from the recrystallization annealing temperature for bi-modal microstructures (fully equiaxed for a cooling rate of 1°C/min), Ti-6242, final heat treatment: 8 h at 595°C

The ductility values of the tensile specimens in Fig. 6.3 were high at room temperature (RA about 40%) and increased to RA values of about 50% at high temperatures. The drastic decline in room temperature ductility at fast cooling rates that was observed for fully lamellar structures (see Fig. 5.18) did not occur for the bi-modal microstructures of the Ti-6242 alloy [6.1] in agreement with the results shown in Fig. 5.20 for the Ti-6Al-4V alloy.

The dependence of high temperature LCF strength at 450°C on cooling rate is shown in Fig. 6.4 for the same material conditions used in Fig. 6.3 (Ti-6242, bi-modal microstructure). In Fig. 6.4 the LCF strength after 10^4 cycles is plotted and it can be seen that the LCF strength shows qualitatively a similar dependence on cooling rate as the yield stress in Fig. 6.3. It should be mentioned again that the LCF strength involves both crack nucleation and microcrack propagation. In Sect. 5.2.1 it was shown for fully lamellar microstructures and room temperature testing that both the resistance to crack nucleation (HCF strength), see Fig. 5.21, and the resistance to microcrack propagation, see Fig. 5.23, were improved with increasing cooling rates. This shows that the discussion in Sect. 5.2.1 on the influence of cooling rate (fineness of the fully lamellar structure) on LCF strength at room temperature also applies for bi-modal microstructures and also for high temperature LCF testing at 450°C (Fig. 6.4), as long as there are no long holding times at peak stress involved in the LCF testing (creep/fatigue interactions).

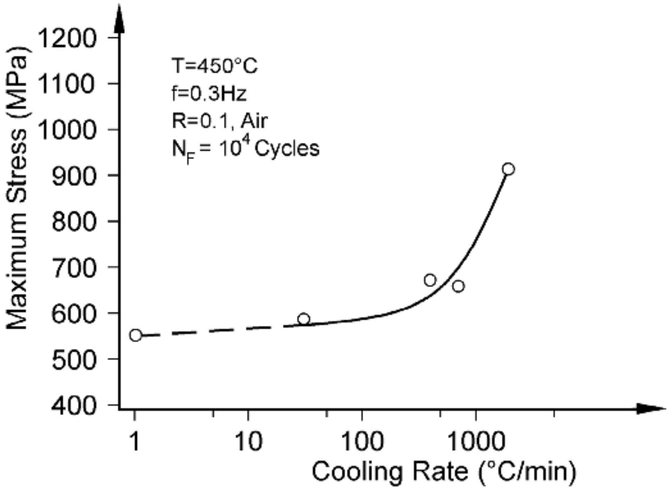

Fig. 6.4. LCF strength at 104 cycles as a function of cooling rate for bi-modal microstructures (same material conditions as in Fig. 6.3), Ti-6242, test temperature: 450°C

Fatigue crack propagation of microcracks and macrocracks at elevated temperatures are usually thought of being no concern because of the high ductility at high temperatures increasing the inherent resistance of the material to crack propagation. But there is a strong environmental effect at elevated temperatures even in laboratory air. An example is shown in Fig. 6.5 comparing for IMI 834 the fatigue crack propagation curves of macrocracks at room temperature and 500°C in vacuum and air [6.2]. It can be seen that the fatigue crack propagation rates in vacuum are only slightly higher at 500°C as compared to room temperature. In contrast, in laboratory air the fatigue crack propagation rates at 500°C in the medium to low ΔK regime are much faster than at room temperature. It was shown that this effect is caused by the presence of water vapor in the environment [6.3]. Typical for the curves at elevated temperatures in such environments is the appearance of a pronounced threshold below which no measurable crack propagation occurs (see Fig. 6.5). A possible explanation for the pronounced threshold is that the protective surface oxide layer at the crack tip is not ruptured by slip steps below a critical ΔK value [6.4] eliminating the transport of hydrogen into the material by dislocations. This hypothesis is supported by a result, which was obtained on an orthorhombic type of titanium alloy, that fatigue crack propagation in vacuum occurred below the threshold value in air, i.e. the two curves were intersecting each other [6.4]. In this case, the residual water vapor in the vacuum caused fatigue crack propagation at very low ΔK values because no protective surface oxide layer at the crack tip was present in the vacuum tests.

The resistance to unstable fracture, i.e. fracture toughness, generally is increased with increasing temperature because the material is more ductile and no environmental effect is present due to the fast crack propagation rate involved.

For high temperature applications, the creep resistance is a very important property in addition to fatigue resistance, especially in the primary creep regime. This is because usually only small plastic creep strains are allowed for many structural components, for example for compressor disks in aero-engines. For all α+β titanium alloys, the plastic creep strain as a function of cooling rate exhibits the characteristic dependence shown in Fig. 6.6 for lamellar structures of the Ti-6Al-4V alloy and in Fig. 6.7 for bi-modal structures of the Ti-6242 alloy. This is true whether the material is cooled from the β phase field (fully lamellar microstructures) or from the recrystallization annealing temperature in the (α+β) phase field (bi-modal microstructure). It is generally observed that the plastic creep strain exhibits a minimum at intermediate cooling rate, approximately between 100-500°C/min. The fully lamellar microstructures (Fig. 6.6) and the bi-modal microstructures (Fig. 6.7) follow the same general trend in creep resistance as a function of cooling rate. This suggests that the possible reasons for the maximum in creep resistance at intermediate cooling rates should pertain to both fully lamellar microstructures and bi-modal microstructures. In the overview of the correlation between microstructure and mechanical properties (Table 5.6) this maximum in creep resistance at intermediate cooling rates is expressed by +/− in the row "Small α Colonies and α Lamellae".

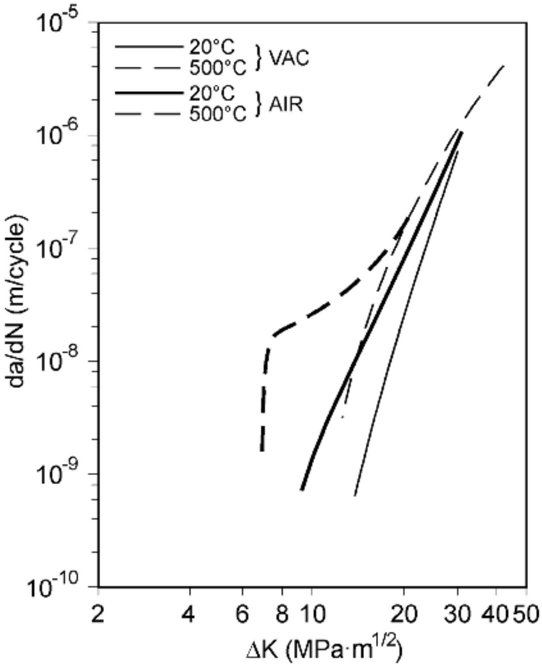

Fig. 6.5. Influence of environment and test temperature on fatigue crack propagation behavior of macrocracks (R = 0.1), IMI 834, bi-modal microstructure

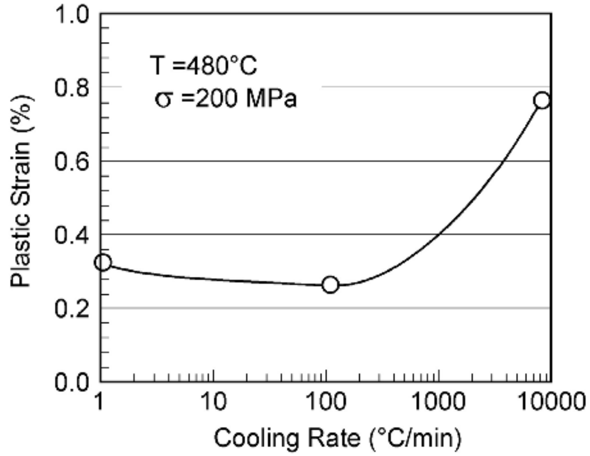

Fig. 6.6. Influence of cooling rate from the β phase field on creep strain after 100 hours for lamellar microstructures of Ti-6Al-4V

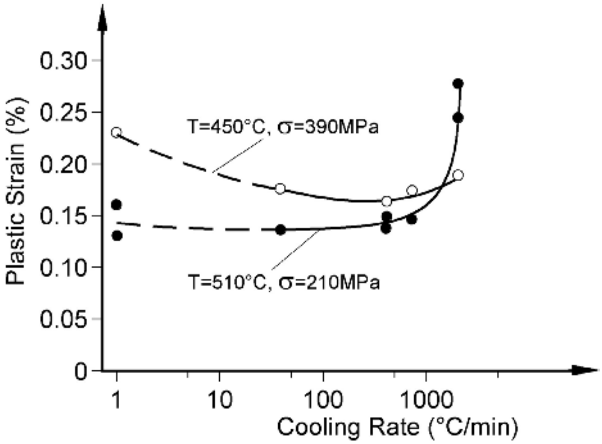

Fig. 6.7. Influence of cooling rate on creep strain after 100 hours for bi-modal microstructures (same material conditions as in Figs. 6.3 and 6.4), Ti-6242

For a discussion of the curves in Figs. 6.6 and 6.7 it is important to realize that the equivalence of slip length and α colony size used up to now in Sects. 5.2 and 6.2, see Fig. 5.17, does not apply for creep deformation. In case of creep deformation the dislocations move, for example by diffusion assisted climb, only over short distances, e.g. across a single α plate, and are annihilated in many cases at the next incoherent boundary, i.e. the α plate boundary.

The decrease in creep resistance with slower cooling rates (Figs. 6.6 and 6.7) is usually explained by the wider α lamellae (plates) leading to larger distances between obstacles for dislocation motion and to lower strain hardening. Another possible explanation is that, because the yield stress is decreasing with decreasing cooling rate, the ratio of applied stress in the creep test to the yield stress at test temperature becomes larger for slower cooled microstructures. The results shown in Fig. 6.7 for the two different stress levels and temperatures are consistent with this explanation because the above mentioned ratio is between 0.7-0.8 for the curve at 450°C (large effect), whereas the ratio is only 0.45 for the curve at 510°C (small effect). The reason for the sharp decrease in creep resistance in the fast cooling rate regime is still unclear. One possibility is that the annihilation process of dislocations at lamellae boundaries dominates over the strain hardening effect because of the large increase in boundary density in microstructures corresponding to faster cooling rates. Since the rate of annihilation of dislocations at lamellae boundaries would be strongly affected by the test temperature because diffusion is involved and less affected by the applied stress, the results in Fig. 6.7 would support this hypothesis, because a sharp decrease in creep resistance in the fast cooling rate regime is observed for 510°C test temperature, whereas only a very small effect is present at a test temperature of 450°C.

A direct comparison of the creep resistance as a function of cooling rate between fully lamellar and bi-modal microstructures is shown in Fig. 6.8 for the IMI 834 alloy. It can be seen that fully lamellar microstructures exhibit a better creep resistance than bi-modal microstructures. This decrease in creep resistance of the bi-modal microstructures with increasing volume fraction of α_p over the whole range of cooling rates shown in Fig. 6.8 can be explained by the alloy partitioning effect in the bi-modal microstructures. The basic strength of the lamellar part of the bi-modal microstructure will become continuously softer with increasing volume fraction of α_p and, in comparison, the reduction in β grain size (α colony size) has no or little influence on the creep resistance as outlined above. At very low volume fractions of α_p (see curve for 4 vol% α_p in Fig. 6.8) the alloy element partitioning effect is not yet in equilibrium, because of the large distances between α_p grains, but the β grain size (α colony size) is already decreased sufficiently for good fatigue properties. This combination of properties cannot be realized in any practical way because the necessary temperature accuracy required during the bi-modal heat treatment to obtain such a low volume fraction of α_p (and the required homogeneity of the material) cannot be achieved in commercial practice.

As outlined in Sect. 5.2.2, the only practical way to partially eliminate the alloy element partitioning effect for bi-modal microstructures seems to be to add an intermediate annealing treatment between the bi-modal recrystallization annealing treatment and the final aging treatment. By such a treatment, for example 2 h at 830°C, it was possible to eliminate the negative influence of the alloying element partitioning effect on HCF strength (see Fig. 5.29). An intermediate annealing treatment of 2 h at 830°C also improves the creep resistance of the bi-modal microstructure with 15 vol% α_p in the slow to medium cooling rate range (Fig. 6.9). This is because the α stabilizing elements such as aluminum and oxygen will diffuse from the primary α into the lamellar α regions during the intermediate annealing treatment. This redistribution of aluminum and oxygen results in a higher volume fraction of Ti_3Al particles in these lamellar α regions upon the final aging treatment of 2 h at 700°C. Consequently, the local yield stress within the lamellar α regions of the bi-modal microstructure is increased resulting in an improved creep resistance. In comparison, the creep resistance of the fully lamellar condition did not change by the intermediate annealing treatment (Fig. 6.9).

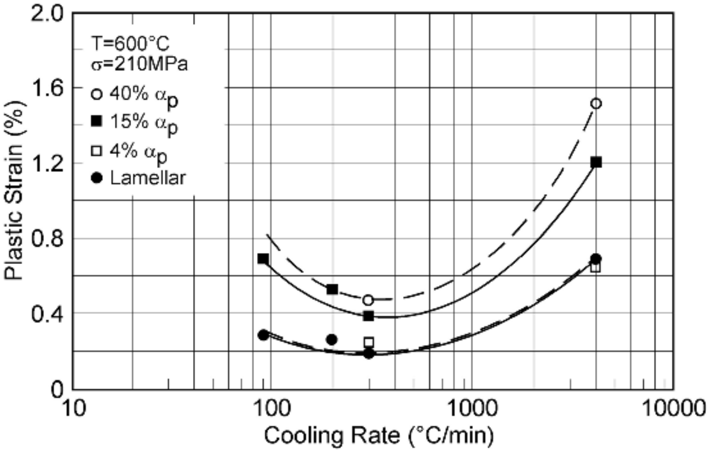

Fig. 6.8. Creep strain after 100 hours as a function of cooling rate for bi-modal and lamellar microstructures of IMI 834

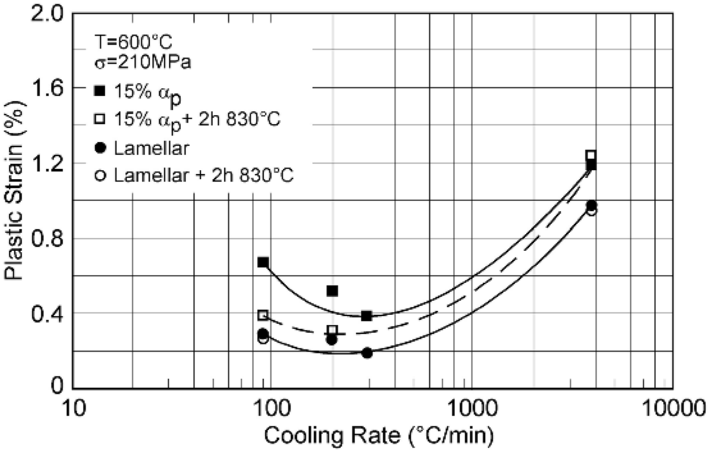

Fig. 6.9. Improvement in creep resistance of a bi-modal structure with 15 vol% α_p by an intermediate annealing treatment of 2 h at 830°C, IMI 834

The influence of α grain size in fully equiaxed microstructures on creep strength of the Ti-6Al-4V alloy is shown in Fig. 6.10. It can be seen that the creep strength is decreasing with decreasing grain size (see also Table 5.6). A drastic decrease in creep resistance is observed for small α grain sizes of about 2-3 µm. The whole curve in Fig. 6.10 is in qualitative agreement with the curves in the medium to fast cooling rate regime of Figs. 6.6 to 6.8. The decrease in creep strength which was observed in the medium to slow cooling rate regime in Figs. 6.6 to 6.8 is not present at large α grain sizes in Fig. 6.10. It should be pointed out that for the fully equiaxed structures in Fig. 6.10 the ratio of applied stress in the creep tests to the yield stress at 480°C was below 0.5.

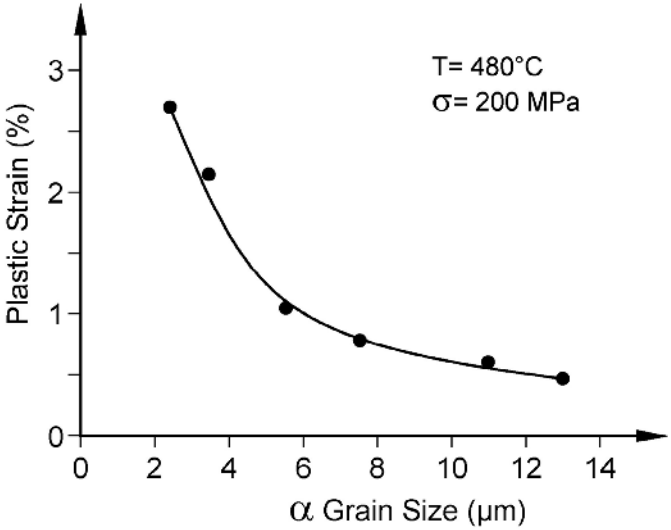

Fig. 6.10. Creep strain after 100 hours as a function of α grain size of fully equiaxed microstructures, Ti-6Al-4V, final aging treatment: 24 h at 500°C

The influence of aging on the creep strength is shown in Fig. 6.11 for the IMI 834 alloy with a bi-modal microstructure [178]. It can be seen that with increasing aging from 2h 625°C to 2h 700°C and to 24h 700°C the creep strength is increasing (see Table 5.6). For reference, the yield stress values at room temperature [6.5] also are included in Fig. 6.11.

The effect of secondary α in the β phase, i.e. the so-called bi-lamellar microstructure, on creep resistance is demonstrated in Fig. 6.12 for the Ti-6Al-4V alloy. The creation of this bi-lamellar microstructure, see as example Fig. 5.44, was discussed in Sect. 5.2.5. The plot in Fig. 6.12 is identical to those shown in Fig. 5.45 for the other mechanical properties, i.e. the creep strain is plotted as a function of cooling rate from the intermediate annealing temperature of 880°C and the starting coarse lamellar microstructure is shown at a cooling rate of 1°C/min. It can be seen from Fig. 6.12 that the bi-lamellar structure exhibited a better creep resistance than the coarse lamellar starting structure, i.e. the hardening of the β phase by secondary α reduced effectively the contribution of the creep strain within the β phase to the total creep strain of the microstructure (see Table 5.6)

The effect of crystallographic texture and test direction on creep strength is directly related to the effect on yield stress (see Table 5.6). This was shown by testing Ti-6Al-4V material with a pronounced T type texture (see Fig. 5.46a) in RD and TD directions [6.6]. The creep resistance was higher in TD direction in agreement with the higher yield stress in this direction at creep testing temperature as well as at room temperature [6.6], see Fig. 5.47b.

All correlations between microstructural parameters and mechanical properties discussed up to now in this section do not depend on Si content of the material because they are valid for Ti-6242 and IMI 834, both containing silicon, as well as for Ti-6Al-4V, containing no silicon. The silicon in Ti-6242 and IMI 834, which is present, as described earlier in this chapter, as $(Ti,Zr)_5Si_3$ particles mainly at α "lamellae" boundaries and also at grain boundaries, raises the absolute creep resistance of these materials as compared to Ti-6Al-4V. However, the silicides, besides improving the creep resistance, also can have a negative effect on mechanical properties, especially on room temperature ductility, if the volume fraction of silicides at α "lamellae" boundaries is too high. This was noted on IMI 834 material after prolonged creep testing (500 h) at 600°C [180]. The room temperature tensile elongation after complete removal of the oxidized layer was reduced from about 10% to about 7% for a bi-modal microstructure. This was attributed to an increase in volume fraction of silicides at the α "lamellae" boundaries [6.7]. For a fully lamellar microstructure with a much lower starting ductility of the virgin material, this drop in ductility would lead to unacceptable low ductility values.

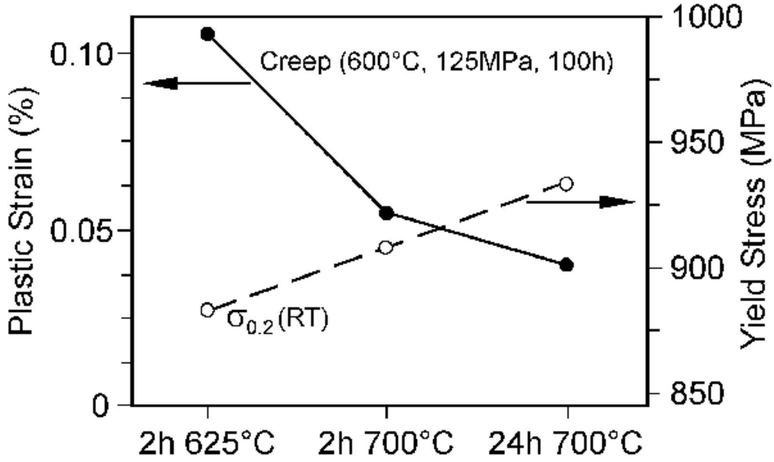

Fig. 6.11. Effect of aging on creep strain after 100 hours for IMI 834 with bi-modal microstructure; also shown are the yield stress values at room temperature

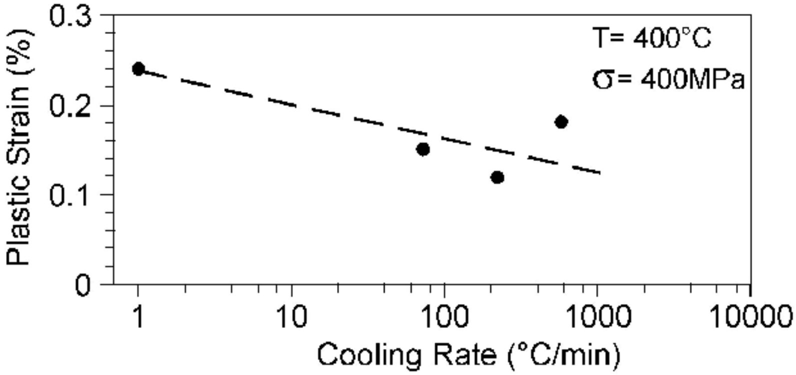

Fig. 6.12. Effect of secondary α in β phase (bi-lamellar microstructure) on creep strain plotting the cooling rate from the intermediate annealing temperature of 880°C (see Fig. 5.45), 1°C/min: lamellar, others: bi-lamellar, Ti-6Al-4V

6.3
Properties and Applications

The main application of high temperature titanium alloys, such as Ti-6242 and IMI 834, are blades and disks in the compressor section of aero-engines. These alloys are applied in the high pressure (HP) compressor stages for which the temperature exceeds 350°C where Ti-6Al-4V cannot be used because of creep considerations.

A good example is the HP compressor spool, shown in Fig. 5.52 and discussed in Sect. 5.3, with five Ti-6Al-4V front stages followed by two Ti-6242 rear stages. Since the maximum temperature capability is about 500°C for Ti-6242 (550°C for IMI 834), the last stages in HP compressors of aero-engines are made out of Ni-Super-Alloys, i.e. in case of the spool example the nickel part is bolted to the titanium part shown in Fig. 5.52. As mentioned already in Sect. 5.3, a bi-modal microstructure is used for the Ti-6242 stages (as well as for the Ti-6Al-4V stages) of the compressor spool, because the LCF strength is the most important mechanical property for this type of application (besides adequate creep strength) and the bi-modal microstructure exhibits better LCF strength than a fully lamellar microstructure (see Fig. 5.31). Recently, Ti-6242 in the fully lamellar condition has been introduced in some applications where creep has become limiting. These fully lamellar structures are produced by β forging creating an elongated unrecrystallized β grain structure (see Sect. 5.1.1 and Fig. 5.5a). This elongated grain shape minimizes the negative effect of the continuous α layers at β grain boundaries on mechanical properties (see detailed discussion in Chap. 7).

Another example for the application of Ti-6242 material with bi-modal microstructure is the impeller shown in Fig. 6.13. Impellers are used as last compressor stage in small, low flow aero-engines and in auxiliary power units (APUs). The impeller shown in Fig. 6.13 has a diameter of 350 mm and is installed in small engines of regional jets, which have several axial stages in between the fan and the impeller.

The newer IMI 834 alloy which can be applied up to about 550°C is used for blades and blisks in the EJ 200 aero-engine [5.25] as well as in the Rolls-Royce TRENT 800 engine. The component shown in Fig. 6.14 is an IMI 834 blisk used in the HP compressor section of the EJ 200 aero-engine. The blisk is manufactured starting with an oversized disk forging and machining out the airfoils at the rim. For the blisk shown in Fig. 6.14 with a diameter of 480 mm the blades are too small for using economically the new technology of solid state linear friction welding to attach the blades to the disk (see Sect. 3.6.2). The IMI 834 alloy is also used as impeller material in the PW 300 engine of PW Canada.

For all these applications of the IMI 834 alloy a bi-modal microstructure with a relatively low volume fraction of α_p (about 15-20 vol%) is used. This microstructure exhibits a very good balance of LCF, HCF, and creep properties. This is because the low volume fraction of α_p reduces the negative alloy element partitioning effect on the latter two properties, see Sect. 5.2.2 (Fig. 5.26) and Sect. 6.2 (Fig. 6.8). Bi-modal microstructures of the Ti-6242 and Ti-6Al-4V alloys, which are usually used with α_p volume fractions of about 35-40%, would also benefit from reducing the volume fraction of α_p, but are difficult to heat treat on industrial scale to lower volume fractions of α_p due to the relatively small annealing temperature "window". In case of IMI 834, this annealing temperature "window" was widened by the addition of 0.06C [6.8, 6.9].

A more detailed list of compressor parts made out of high temperature titanium alloys including the "older" alloys IMI 685 and IMI 829 can be found elsewhere [5.25, 5.26].

Fig. 6.13. Impeller used in a small engine for regional jets, Ti-6242, bi-modal microstructure (courtesy J. A. Hall, Honeywell Engines and Systems)

Fig. 6.14. High pressure compressor blisk used in the EJ 200 aero-engine, IMI 834, bi-modal microstructure (courtesy D. Helm, MTU)

6.4
Recent Developments since the First Edition

6.4.1
Dwell Fatigue

The phenomenon of dwell fatigue described here is most pronounced at ambient temperature and essentially vanishes at about 200°C. It mainly occurs in the high temperature alloys which are the subject of this chapter. Therefore, this effect is discussed here even though it is not a high temperature effect.

High temperature α+β titanium alloys such as Ti-6242, IMI 685, and IMI 834 can exhibit a significant reduction in fatigue life during tests when the load is held at maximum value instead of being continuously cycled. This reduction also is characterized by subsurface crack initiation and the failure mode in the origin area is a faceted fracture [6.10] with the facet planes lying near $(0002)_\alpha$ and having an orientation that is nearly normal to the loading axis (significantly removed from a maximum shear stress orientation). The phenomenology of dwell fatigue is well documented but the detailed failure mechanism is still undergoing investigation. Consequently, the focus of this discussion will be on the phenomenology of dwell fatigue. The principal features of dwell fatigue include the following:

- Alloy effects.
- Microstructure effects.
- Loading effects.
- The effect of room temperature creep.
- Fracture behavior.

Each of these features will be discussed separately.

It is common to express the sensitivity to dwell fatigue using the ratio of the life during continuous cycling to the life during a dwell test. This ratio is termed the dwell fatigue debit. The magnitude of the debit can range from a low value of nearly one for unsusceptible alloys and alloy conditions to > 10 for highly susceptible conditions. Clearly, an order of magnitude reduction in fatigue life is the cause for major concern.

The literature on dwell fatigue suggests a strong connection between alloy composition and dwell fatigue debit. In particular, the high temperature α+β alloys with very low volume fractions of β phase such as Ti-6242, IMI 685, IMI 829, and IMI 834 (see Chap. 2, Table 2.6) are the most susceptible alloys to dwell fatigue. The commonly used α+β and β alloys such as Ti-6Al-4V, Ti-6246, and Ti-17 exhibit a much lower effect or no susceptibility at all. This is illustrated for Ti-6246 in Fig. 6.15.

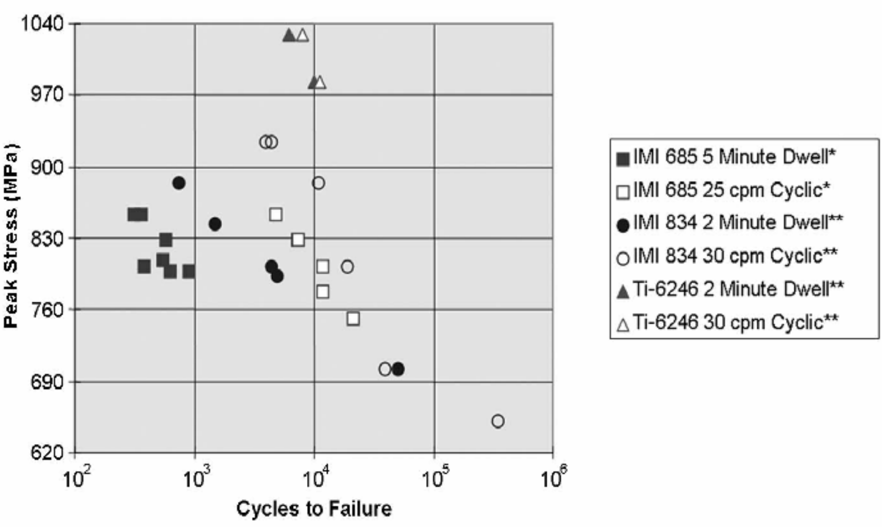

Fig. 6.15. S-N curves with and without dwell time for three titanium alloys showing the variation in dwell fatigue susceptibility as a function of alloy and stress level, *[6.11] **[6.12]

The microstructural condition in a particular alloy also affects the extent of the dwell fatigue debit. Four microstructural conditions in Ti-6242 are shown in Fig. 6.16a-d. The dwell fatigue debit values corresponding to these microstructures are shown in Table 6.1. The most important microstructural feature with regard to dwell fatigue sensitivity is microtexture (see Sects. 3.9.1 and 3.9.2). Microtexture consists of regions within the microstructure having a common orientation of the α phase. Microtexture is developed during processing to create an α+β structure if temperatures and strains are used that allow the orientation of the prior α+β colony structure to persist. One of the reasons for the historic occurrence of dwell fatigue is that optical bright field images do not provide insight into the presence of microtexture (see Fig. 3.80). Orientation imaging microscopy in the SEM (Fig. 3.91) allows the nature and extent of microtexture to be quantified but this technique is time consuming, requires sophisticated instrumentation and therefore is expensive to use.

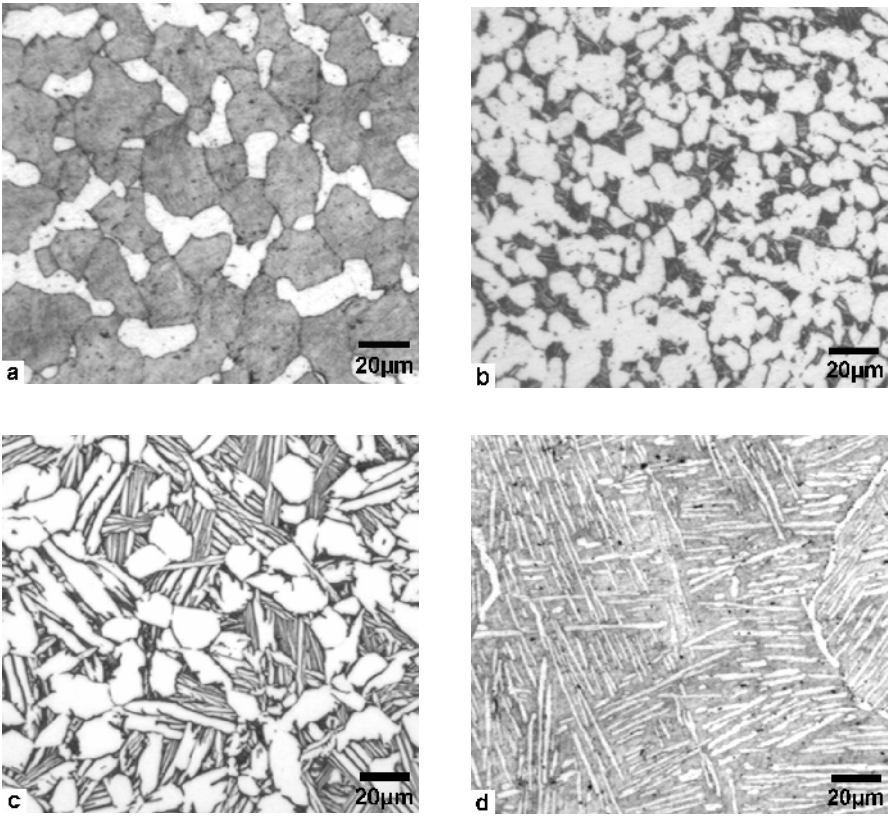

Fig. 6.16. Four microstructures of Ti-6242 with varying degree of microtexture and dwell fatigue susceptibility: (a) α+β forged with minimum microtexture (b) α+β forged with high microtexture (c) α+β forged with high microtexture representative of material produced in the 1980's time frame (d) β forged

The severity of the dwell fatigue life debit depends on the dwell period and on the maximum stress level. Increasing the dwell time up to about 2 minutes leads to increasingly large fatigue life reductions compared to continuous cycling. Tests using dwell times longer than 2 minutes cause minimal further increase in life debit. The observations on dwell time effect at very long times are relatively few because the total time required to run tests with long dwell times is considerable (for example, a 10 000 cycle test with 5 min dwell lasts about 35 days), making the test very expensive. It also has been shown that the dwell debit has a strong stress dependence as can be seen in Fig. 6.15 by comparing the IMI 834 behavior when tested with and without dwell time at high and low peak stress values. As a consequence, most of the available data for dwell fatigue corresponds to tests run at high stresses (but less than the 0.2% yield stress). The stresses used in laboratory dwell fatigue tests are considerably higher than the operating stress in rotors of gas turbine engines, nevertheless dwell fatigue failures have been experienced during service. This apparent paradox is an ongoing source of concern for makers and operators of gas turbine engines and is an inducement to understand the underlying mechanism of dwell fatigue sensitivity.

Table 6.1. Dwell fatigue debit values for the four microstructures shown in Fig. 6.16, Ti-6242 [6.10]

Material	R-Value	σ_{MAX} (MPa)	Dwell Time	N_F	Dwell Fatigue Debit
Pancake Forging #1	0.1	870	1 minute	>32 684	
(Random),	0.1	870	No-dwell	160 031	>4.9
Fig. 6.16a					
Pancake Forging #2	0.1	870	1 minute	4 097	
(High Microtexture),	0.1	870	No-dwell	37 724	9.2
Fig. 6.16b					
1980's Vintage Material	0	870	2 minutes	2 492	
(α+β Forged),	0	870	No-dwell	27 755	11
Fig. 6.16c					
Pancake Forging #3	0	917	2 minutes	11 887	
(β Forged)	0	917	No-dwell	30 197	2.5
Fig. 6.16d					

Room temperature creep of titanium alloys has been recognized for quite some time [6.13, 6.14]. Until the issue of dwell fatigue became important, the main implication of room temperature creep was dimensional stability of highly stressed components. More recently, the role of creep in the occurrence of time dependent internal stress redistribution has been recognized and has been modeled using finite element and crystal plasticity methods that incorporate time dependent strain [6.15, 6.16]. The creep appears to be exhaustive with the total creep strain approaching an asymptotic value after times on the order of minutes. Both the maximum plastic strain and the time required to achieve this are stress dependent with the strains increasing and the times decreasing for higher stresses (all below the macroscopic yield stress). A typical creep strain versus time plot is shown in Fig. 6.17 [6.17]. The propensity for creep is recoverable as was determined by unloading the specimen and allowing it to sit at ambient temperature for 11 months before reloading. The high creep rate after reloading also is shown in Fig. 6.17. The implications of this recovery on dwell fatigue are not completely understood at present.

As mentioned earlier, the dwell fatigue crack initiation sites are characterized by flat facets that occur at subsurface locations [6.10]. An example of such an origin is shown at low magnification in Fig. 6.18a, whereas Fig. 6.18b shows the details of faceted crack growth observed near the origin. The facets have a physical orientation very nearly normal to the loading axis and the plane of the facet is consistently within a few degrees of $(0002)_\alpha$ [6.18]. Faceted fracture such as that shown in 6.18b is commonly observed near the origin in Ti fatigue failures and are consistent with fatigue crack growth at low ΔK values. As the crack grows and ΔK increases, the fracture mode changes into striation growth, as illustrated in Fig. 6.19. The principal difference between dwell fatigue cracks and ordinary fatigue cracks is that the dwell crack initiation sites are always much closer to a maximum normal stress orientation than to a maximum shear stress orientation.

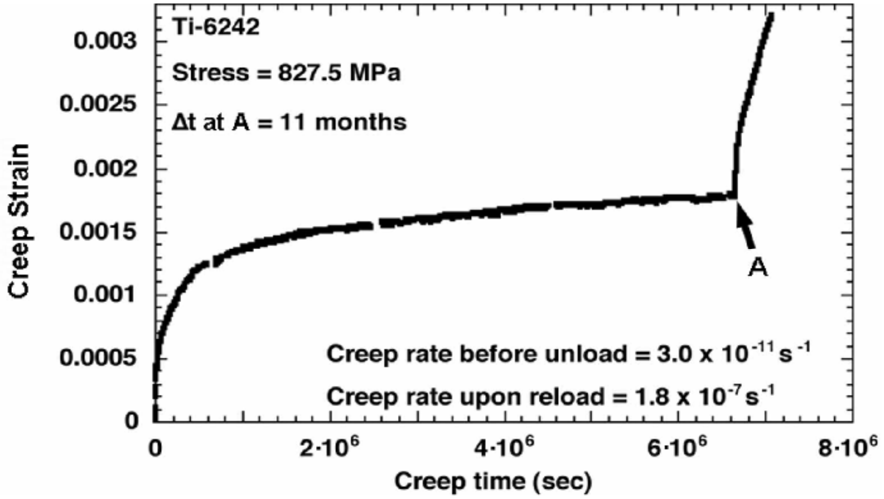

Fig. 6.17. Plot of creep strain versus time at room temperature, point A indicates the creep rate on reloading after long unloading period at room temperature [6.17]

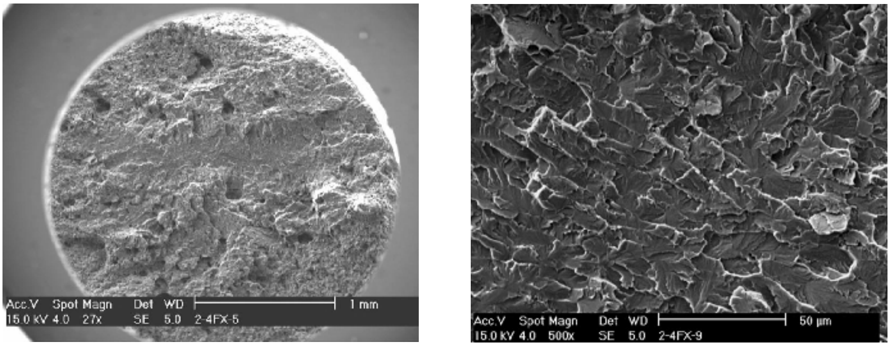

a **b**

Fig. 6.18. Fracture surface of a Ti-6242 dwell fatigue specimen: (a) Low magnification image showing subsurface crack initiation (b) Higher magnification image taken near crack initiation site showing faceted fracture during dwell fatigue crack growth [6.10]

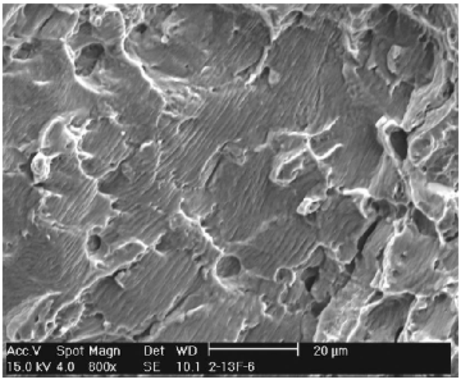

Fig. 6.19. Fracture surface of a Ti-6242 dwell fatigue specimen taken well away from crack initiation location showing striation crack growth [6.10]

Considerable effort has been expended on modeling dwell fatigue failure and this has led to an improved conceptual understanding of this failure mode. Qualitatively, the basic cause of the dwell fatigue debit is related to the elastic and plastic anisotropy of the α phase which leads to hard and soft regions in the microstructure. This anisotropy, when coupled with the propensity of α+β alloys to creep at ambient temperature, leads to internal stress redistributions in the material when the load is held at maximum value. The creep, particularly under constant load conditions, and the attendant load redistributions can create regions with high enough stresses to initiate a crack. The propensity to form a crack becomes greater as the size of the hard region increases and as the size of surrounding soft regions increases or as these soft regions become weaker because they are favorably oriented for slip. Because the stress redistribution between soft and hard regions is time dependent, the rate depends on the stress exponent m in the creep equation and the applied stress. It is curious that this failure mode is triggered by a hold time, yet there are models of this phenomenon that do not incorporate time dependence.

There has been a significant effort to model dwell fatigue using the methods of solid mechanics including finite element and crystal plasticity methods. These models have corroborated the concept of internal load redistribution to hard regions in the microstructure and provide quantitative values. Figure 6.20 shows the finite element model of a microstructure which contains a hard region at the center surrounded by soft matrix. Using experimentally determined relations that capture the elastic and plastic anisotropy of the α phase and incorporate time dependence into the models it has been shown that high stresses develop at the boundaries of the hard regions (shown in Fig. 6.20 as dark areas at top and bottom and marked by an A). The constitutive relations used in this model were experimentally obtained from micro tensile tests on single colony specimens of Ti-6242. The time dependence was obtained from actual room temperature creep measurements of Ti-6242. The amplification of the local stress that occurs at the boundary between the hard and soft regions is shown graphically in Fig. 6.21. The curves in this figure show the effect of varying the stress exponent m in the creep equation between 0.02 and 0.05. This also demonstrates that the more rapidly the material creeps, the higher the stress build-up is after a given hold time.

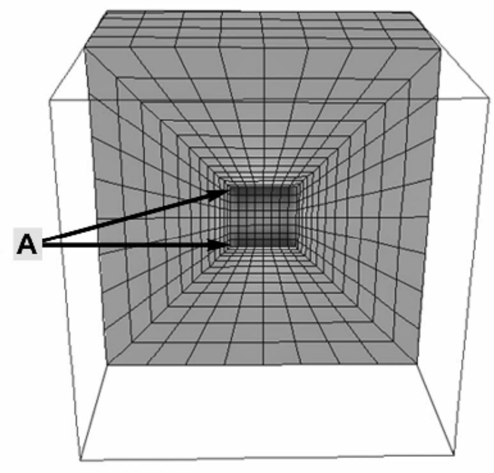

Fig. 6.20. Finite element map used in modeling load distribution during dwell fatigue loading of plastically inhomogenous material, high stress areas in hard region denoted by A [6.15]

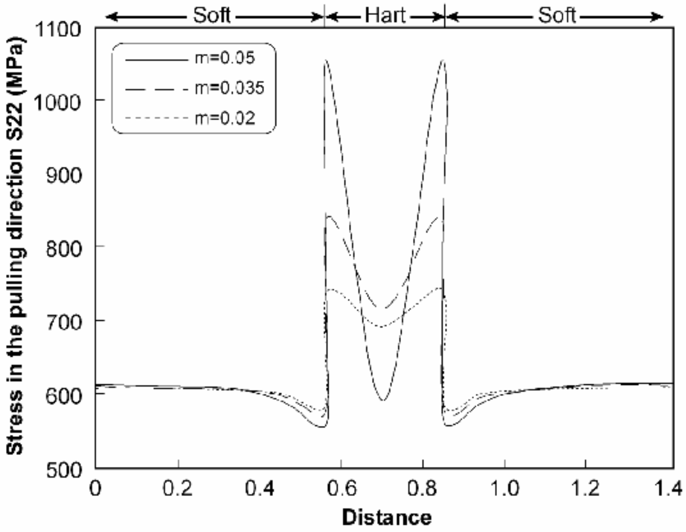

Fig. 6.21. Plot of local stress versus distance showing large increase in stress at boundary between hard and soft regions in microstructure [6.15]

While this modeling effort has been very useful in providing quantitative support for the qualitative ideas regarding the cause of dwell fatigue with more quantitative information, the ability to predict crack initiation is still not possible. This is in part because the present models do not incorporate microstructural length scales. This is the focus of continuing studies. Further, since the constitutive relations and creep behavior used in modeling Ti-6242 are experimentally obtained, modeling of other alloys will require a significant parallel experimental effort.

The effect of dwell loading during the growth of macrocracks has been determined. It appears that there is essentially no difference in the crack growth rate between continuously cycling and when there is a hold time at maximum load. This leads to the conclusion that the dwell effect is mainly related to accelerated crack initiation and growth of microcracks during dwell testing.

The occurrence of dwell fatigue poses a serious problem for the producers and operators of aircraft engines. In part this is because continuously cycling tests are the usual means of fatigue testing titanium alloys to obtain data used in rotor design. As mentioned earlier, these tests produce nonconservative life estimates if dwell fatigue is a possible cause of failure. The consequences of a rotor burst during service are not acceptable and, consequently, periodic inspections of rotors currently are required during service. In a few instances, these inspections have resulted in identification of cracks requiring the removal of the rotor. Subsequent analysis of these cracks has led to the conclusion that they were caused by dwell fatigue. Since the rotors operate at significantly lower stresses than the stresses used in laboratory dwell tests, the stress dependence shown in Fig. 6.15, while correct for laboratory specimens, does not appear to represent the situation in large rotating parts. Any model that successfully represents dwell fatigue accurately will have to demonstrate the capability to account for this apparent discrepancy between field experience and laboratory experiments. While the response to this challenge is not currently available, it is likely that the model will be required to include probabilistic features to capture the observed variation in dwell sensitivity as a function of stressed volume.

6.4.2
Effect of Ni Impurities on Creep Strength

Recently, it has been noticed that there is considerable variation in the creep strength of Ti-6Al-2Sn-4Zr-2Mo. Attempts to account for this on the basis of microstructure have been unsuccessful. Consequently, detailed evaluations of different heats of material show that a qualitative correlation exists between creep behavior and variations in the concentration of the minor impurity Ni. Similar variations also appear to apply to other impurities such as Fe and Co, all at the trace impurity level. The effect of Fe has been recognized for some time [6.19] and the Fe concentration is deliberately and effectively managed by the material producers in Ti-6242 and other high temperature alloys in order to optimize creep strength. This is mainly accomplished by selecting low Fe sponge for alloy formulation. Impurities of Ni and Fe are particularly troublesome in titanium production because of the use of Ni containing stainless steel vessels in the Kroll reactors for making sponge and for vacuum distillation of the sponge after reduction, as shown in Fig. 3.3. Further, the current practice worldwide involves the use of vacuum distillation as opposed to acid leaching for salt removal from the sponge, see Sect. 3.1. Thus, literally all sponge produced today has been exposed to Ni bearing alloys during production, making trace concentration of Ni unavoidable. There also is a qualitative correlation between the timeframe when degradation of creep strength of Ti-6242 became an issue and the transition from acid leaching to the general use of vacuum distillation.

The reduction in creep capability in the temperature range 475-550°C is important enough to the aero-engine manufacturers that several research efforts have been initiated to provide a more fundamental understanding of the "Ni effect". As a consequence, several interesting and occasionally conflicting conclusions regarding this effect can be found in the literature. In the case of alloys such as Ti-6242, the first question is whether the role of Fe and Ni is to affect the creep characteristics of the α or the β phases. Based on the knowledge that these elements have very limited solubility in the α phase, early reports basically assumed that the β phase was primarily affected [6.19, 6.20]. More recently, studies on Ti-6242 and on Ti-6Al binary alloys containing different levels of Ni (with small variations in Fe content also) have shown that Ni has a large effect on creep strength in both the binary and the α+β alloy [6.21, 6.22]. Since the binary alloy contains no β phase, the earlier assumptions regarding the role of the β phase clearly are called into question. As briefly described in Sect. 2.9.1, the Herzig group at the University Muenster in Germany [2.35, 6.23] has studied the diffusion of Ni, Fe, and Co in the α phase and has found anomalously fast self-diffusion rates when these impurities are present even in trace amounts (1.7 ppm). Similar effects of Fe impurities on self-diffusion in α Zr also have been reported [6.24]. The Herzig group attributes this anomalously high diffusion rate to the diffusion of these impurities as interstitials rather than as substitutional atoms. They offer an explanation for this surprising assertion based on the large ratio of ionic to atomic radii characteristic of "open" HCP metals such as Ti, Zr, and Hf. This assertion is supported by the measured large reduction in activation energy for self-diffusion between ultra pure α titanium and α titanium containing a few ppm of Ni. In ultra pure α titanium the activation energies are consistent with normal vacancy diffusion. In the presence of Fe, Ni, or Co in very small concentrations, this activation energy is reduced to lower values leading to the suggestion of interstitial diffusion. The exact mechanism of this accelerated diffusion is still an open issue.

Returning to the variation in creep behavior, it has been shown that increasing the Ni impurity level from 0.005% to 0.035% in Ti-6242 causes a large reduction in creep strength as shown in Fig. 6.22 [6.21]. The activation energy for creep in the low Ni material compares favorably to the activation energy for intrinsic (vacancy) self-diffusion in α titanium. This suggests a diffusion controlled creep mechanism. Detailed TEM studies of dislocation structures after creep show that creep occurs mainly by the motion of $\vec{a}$ type dislocations in the α phase [6.22]. Further, detailed examination of the β phase after creep deformation shows very few dislocations suggesting that creep is dominated by deformation of the α phase. Dislocation loops and large jogs on screw dislocations were prevalent in the as-crept specimens and this type of substructure is consistent with nonconservative (diffusion controlled) motion of these dislocations. Figures 6.23 and 6.24 show Arrhenius plots of minimum creep rate as a function of temperature for different stress levels for the materials with two levels of Ni impurities (0.005% and 0.035%) [6.21]. Since the slopes of these curves are the activation energies for creep, it appears that increased Ni concentration, even in small overall amounts, decrease the average activation energy from about 330 kJ/mole (Fig. 6.23) to about 280 kJ/mole (Fig. 6.24) over the range of stresses and temperatures investigated. This reduction in activation energy for creep qualitatively accounts for the reduced creep resistance of Ti-6242 with increasing Ni impurity levels.

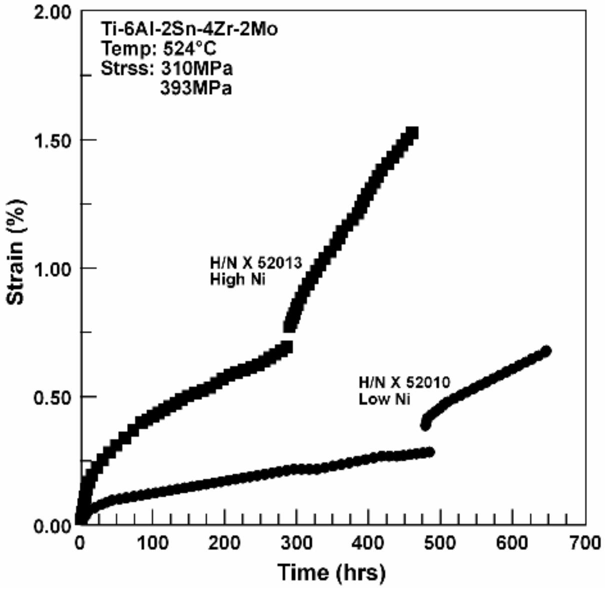

Fig. 6.22. Creep strain for two stress levels as a function of time for Ti-6242 containing two different levels of Ni impurity (0.005% and 0.035%) [6.21]

Based on the foregoing discussion, it appears that the detrimental effect of Ni impurities on creep is caused by the effect of these impurities on diffusion in the α phase. Moreover, diffusion controlled dislocation motion in the α phase has been shown to be the rate controlling creep mechanism. Consistent improvement in the creep strength of high temperature alloys such as Ti-6242 will therefore require the use of material with as low Ni levels as can be feasibly achieved commercially.

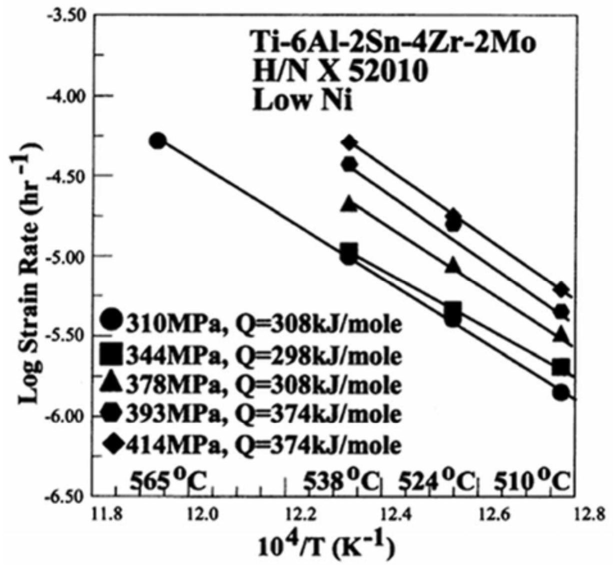

Fig. 6.23. Arrhenius plot of minimum creep rate for five stress levels, Ti-6242 with 0.005% Ni (low Ni) [6.21]

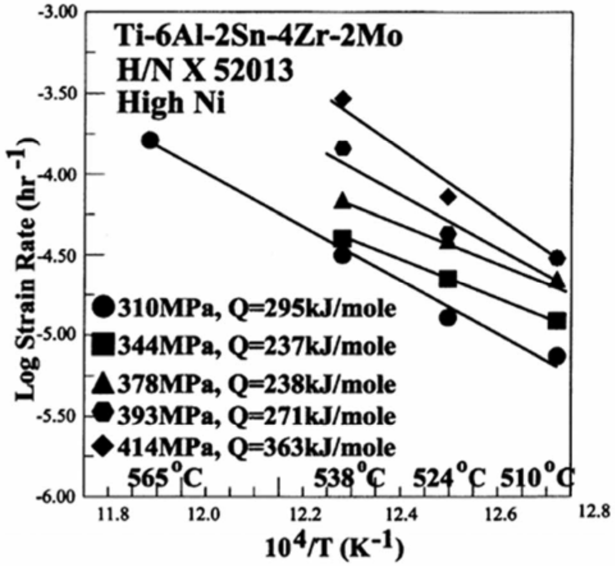

Fig. 6.24. Arrhenius plot of minimum creep rate for five stress levels, Ti-6242 with 0.035% Ni (high Ni) [6.21]